INTERNATIONAL JOURNAL FOR NUMERICAL METHODS IN FLUIDS
Int. J. Numer. Meth. Fluids **28**: 143–156 (1998)

A NUMERICAL STUDY ON FLOW THROUGH THE SPIRAL CASING OF A HYDRAULIC TURBINE

G. BISWAS*, V. ESWARAN, G. GHAI AND A. GUPTA[1]

Department of Mechanical Engineering, Indian Institute of Technology, Kanpur 208 016, India

SUMMARY

Flow through the spiral casing of a hydraulic turbine was analyzed. Reynolds averaged Navier–Stokes equations were solved using a finite element method. The physical domain was divided into a number of hexahedral elements which are isoparametrically mapped onto standard cubic elements. Numerical integration for the unsteady momentum equation is performed over such hexahedral elements to obtain a provisional velocity field. Compliance with the mass conservation equation and determination of the pressure correction are accomplished through an iterative procedure. The velocity distribution inside the spiral casing corroborates the results available in literature. The static pressure at the midplane generally decreases from the outside wall towards the exit of the spiral casing. © 1998 John Wiley & Sons, Ltd.

KEY WORDS: turbine; spiral casing; finite element method; Galerkin weighted residual technique; Gauss–Legendre quadrature

1. INTRODUCTION

The spiral casing is a passage with a 360° turn, directing the water which enters at one end to exit circumferentially along the radial inward direction (Figure 1). The role of the spiral casing in a Francis or Kaplan turbine is to distribute the water, as evenly as possible, to the stay vanes and wicket gates (guide vanes) and then to the turbine runner. In a good spiral casing the pressure head of the fluid is made available to the runner with minimum loss, hence the analysis of the flow through a spiral casing is important for efficient design of hydraulic turbines. Very few articles are available in the open literature on the computational analysis of this problem. The investigations carried out by Ulrich [1], Vu and Shyy [2,3], Shyy and Vu [4], Mrsa [5] and Soares *et al.* [6] are considered pioneering work. In the present work, a detailed numerical simulation of turbulent flow through a spiral casing has been attempted. The simulation is to predict the flow structure and pressure drop characteristics in a type of spiral casing generally used for Francis turbines. For the modeling of turbulent flow, a zero-equation (mixing length) model has been used. The zero-equation models obviously have several shortcomings which are indicated in the turbulent flow literature. The basic flow itself is extremely complex, therefore, the turbulence aspect has been dealt with using a simple model at this stage. Despite this simplification, the simulation proves to be a useful design tool for the spiral casing.

* Correspondence to: Department of Mechanical Engineering, Indian Institute of Technology, Kanpur 208 016, India.
[1] Present address: Flow Consultants India, Pune 412 114, India.

CCC 0271–2091/98/110143–14$17.50

Received June 1996
Revised January 1997

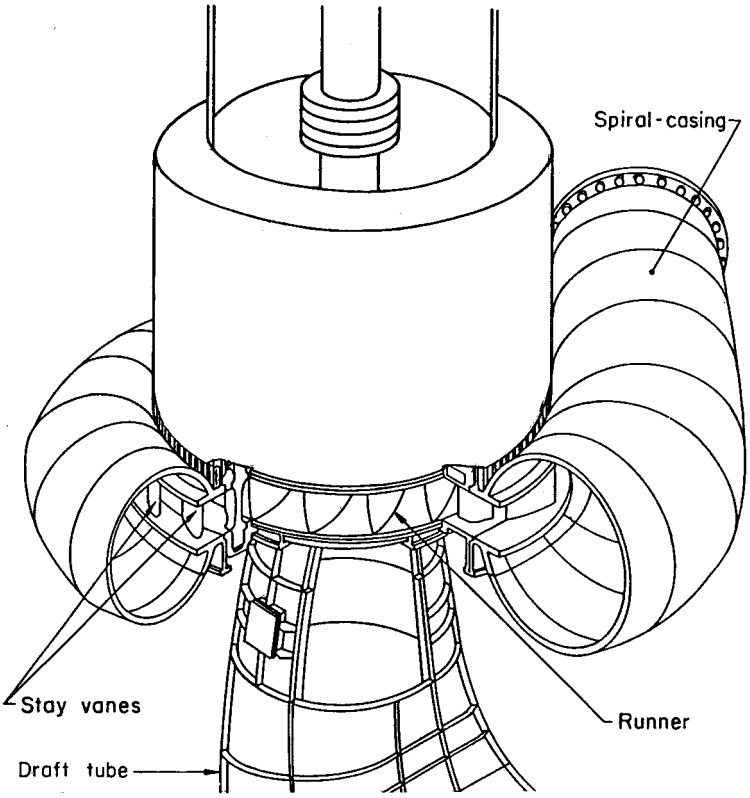

Figure 1. Spiral casing of a hydraulic turbine.

2. MATHEMATICAL FORMULATION

2.1. Flow model and the grid system

In this study, a finite element approach [7] has been adopted to solve the flow in the spiral casing. A structured grid has been generated through transfinite interpolation. This technique [8] is easy to implement and allows explicit control over grid spacing. The three-dimensional grids are formed by generating two-dimensional grids over each cross section and connecting these in the axial direction. Figure 2 shows the grid of the spiral casing.

2.2. Domain discretization and governing equations

As discussed in the earlier section, the domain is discretized into small curvilinear hexahedral elements (Figure 2). The velocity components and the pressure are collocated at each node of the element. The Reynolds averaged Navier–Stokes equations for incompressible flows, with the Reynolds stresses modeled via eddy-viscosity concepts, have been used here as governing equations. These equations can be written in a Cartesian tensor form as

$$\frac{\partial u_j}{\partial x_j} = 0, \tag{1}$$

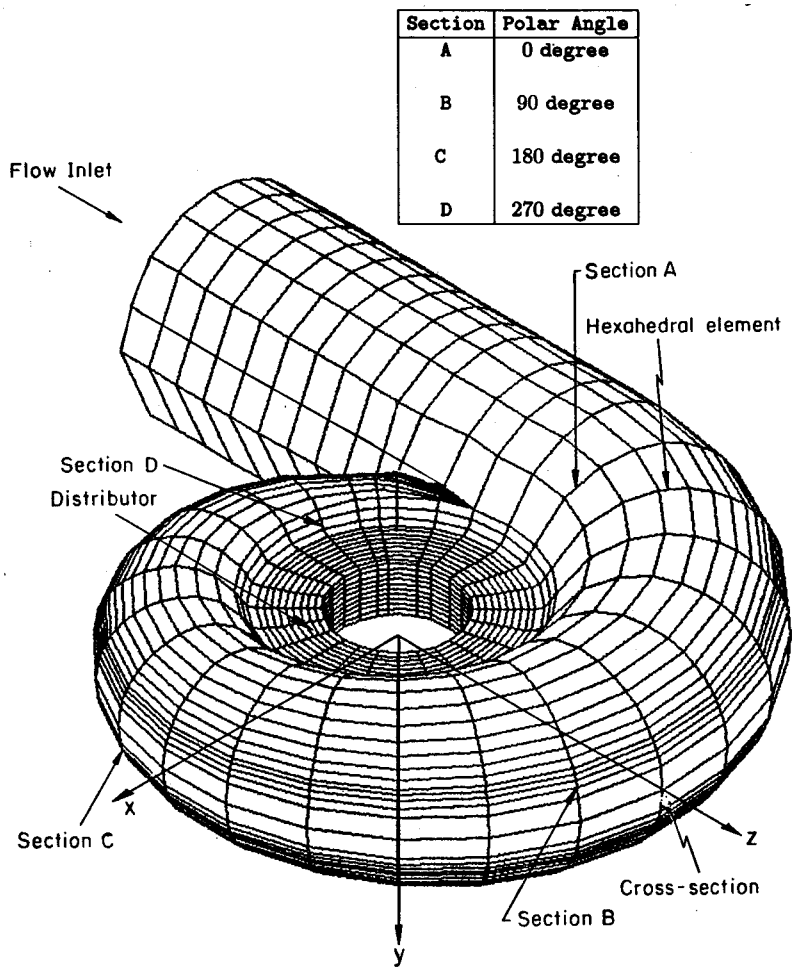

Figure 2. Grid for the spiral casing.

$$\frac{Du_j}{D\tau} = -\frac{\partial p}{\partial x_j} + \frac{1}{Re}\frac{\partial}{\partial x_i}\left[(1+\nu_{t,n})\left(\frac{\partial u_i}{\partial x_j}+\frac{\partial u_j}{\partial x_i}\right)\right]. \tag{2}$$

The subscripts i and j can take the values 1, 2 or 3 for the three Cartesian co-ordinate directions as x_1, x_2 and x_3 respectively. The equations have been written in the dimensionless form, which facilitates generalization to embody a large range of problems. Here

$$Re = W_0 D/\nu,$$

where D is the diameter at the inlet of the spiral casing, ν is the kinematic viscosity and W_0 is the inlet velocity. The non-dimensional turbulent viscosity $\nu_{t,n}$ is given by Prandtl's mixing length model as

$$\nu_{t,n} = l_n^2 Re\left[\left(\frac{\partial u_i}{\partial x_j}+\frac{\partial u_j}{\partial x_i}\right)\frac{\partial u_i}{\partial x_j}\right]^{1/2}. \tag{3}$$

In the above equation, l_n is given by $\lambda\delta$, where δ is the non-dimensional radius of the duct at any section and λ is a constant (chosen as 0.09). Equations (1) and (2) can be written in full, using (x, y, z) and (u, v, w) instead of (x_1, x_2, x_3) and (u_1, u_2, u_3).

Continuity equation

$$\frac{\partial u}{\partial x}+\frac{\partial v}{\partial y}+\frac{\partial w}{\partial z}=0. \tag{4}$$

x-momentum equation

$$\frac{\partial u}{\partial \tau}+u\frac{\partial u}{\partial x}+v\frac{\partial u}{\partial y}+w\frac{\partial u}{\partial z}=-\frac{\partial p}{\partial x}+\frac{1}{Re}\left[\frac{\partial}{\partial x}\left\{(1+\nu_{t,n})\left(2\frac{\partial u}{\partial x}\right)\right\}+\frac{\partial}{\partial y}\left\{(1+\nu_{t,n})\left(\frac{\partial v}{\partial x}+\frac{\partial u}{\partial y}\right)\right\}+\frac{\partial}{\partial z}\left\{(1+\nu_{t,n})\left(\frac{\partial w}{\partial x}+\frac{\partial u}{\partial z}\right)\right\}\right]. \tag{5}$$

y-momentum equation

$$\frac{\partial v}{\partial \tau}+u\frac{\partial v}{\partial x}+v\frac{\partial v}{\partial y}+w\frac{\partial v}{\partial z}=-\frac{\partial p}{\partial y}+\frac{1}{Re}\left[\frac{\partial}{\partial x}\left\{(1+\nu_{t,n})\left(\frac{\partial u}{\partial y}+\frac{\partial v}{\partial x}\right)\right\}+\frac{\partial}{\partial y}\left\{(1+\nu_{t,n})\left(2\frac{\partial v}{\partial y}\right)\right\}+\frac{\partial}{\partial z}\left\{(1+\nu_{t,n})\left(\frac{\partial w}{\partial y}+\frac{\partial v}{\partial z}\right)\right\}\right]. \tag{6}$$

z-momentum equation

$$\frac{\partial w}{\partial \tau}+u\frac{\partial w}{\partial x}+v\frac{\partial w}{\partial y}+w\frac{\partial w}{\partial z}=-\frac{\partial p}{\partial z}+\frac{1}{Re}\left[\frac{\partial}{\partial x}\left\{(1+\nu_{t,n})\left(\frac{\partial u}{\partial z}+\frac{\partial w}{\partial x}\right)\right\}+\frac{\partial}{\partial y}\left\{(1+\nu_{t,n})\left(\frac{\partial v}{\partial z}+\frac{\partial w}{\partial y}\right)\right\}+\frac{\partial}{\partial z}\left\{(1+\nu_{t,n})\left(2\frac{\partial w}{\partial z}\right)\right\}\right]. \tag{7}$$

The turbulent viscosity $\nu_{t,n}$ is obtained from Equation (3).

Boundary conditions

Dirichlet and Neumann boundary conditions have been made use of. These are

- on the solid wall surfaces

$$u=0, \qquad v=0, \qquad w=0; \qquad \frac{\partial p}{\partial n}=0,$$

- at the inflow plane

$$u=0, \qquad v=0, \qquad w=W_0; \qquad \frac{\partial p}{\partial n}=0,$$

- at the exit boundary

$$\frac{\partial u}{\partial n}=0, \qquad \frac{\partial v}{\partial n}=0, \qquad \frac{\partial w}{\partial n}=0; \qquad p=p_{\text{atm}}$$

where n signifies normal direction.

2.3. Solution of transport equations

Galerkin's weighted residual method [7] has been used to derive the matrix equations for the nodal values of velocity and pressure. Applying Galerkin's technique to Equation (5) gives

$$\iiint_{\forall} N_i\left[\frac{\partial u}{\partial \tau}+u\frac{\partial u}{\partial x}+v\frac{\partial u}{\partial y}+w\frac{\partial u}{\partial z}+\frac{\partial p}{\partial x}-\frac{(1+v_{\text{t,n}})}{Re}\{\nabla^2 u\}\right.$$
$$\left.-\frac{1}{Re}\left\{2\frac{\partial u}{\partial x}\frac{\partial v_{\text{t,n}}}{\partial x}+\left(\frac{\partial v}{\partial x}+\frac{\partial u}{\partial y}\right)\frac{\partial v_{\text{t,n}}}{\partial y}+\left(\frac{\partial w}{\partial x}+\frac{\partial u}{\partial z}\right)\frac{\partial v_{\text{t,n}}}{\partial z}\right\}\right]\mathrm{d}x\ \mathrm{d}y\ \mathrm{d}z=0, \quad i=1,2,\ldots,m.$$

The application of Green's theorem results in

$$\iiint_{\forall} N_i\,\dot{u}\ \mathrm{d}x\ \mathrm{d}y\ \mathrm{d}z$$

$$=-\iiint_{\forall}\underbrace{N_i\left\{u\frac{\partial u}{\partial x}+v\frac{\partial u}{\partial y}+w\frac{\partial u}{\partial z}\right\}}_{\text{conv } u}\mathrm{d}x\ \mathrm{d}y\ \mathrm{d}z$$

$$-\iiint_{\forall}\underbrace{N_i\left\{\frac{\partial p}{\partial x}\right\}}_{\text{pgrd}u}\mathrm{d}x\ \mathrm{d}y\ \mathrm{d}z+\iint_{s}N_i\frac{(1+v_{\text{t,n}})}{Re}\frac{\partial u}{\partial n}\mathrm{d}s$$

$$-\iiint_{\forall}\underbrace{\frac{(1+v_{\text{t,n}})}{Re}\left\{\frac{\partial N_i}{\partial x}\left(2\frac{\partial u}{\partial x}\right)+\frac{\partial N_i}{\partial y}\left(\frac{\partial u}{\partial y}+\frac{\partial v}{\partial x}\right)+\frac{\partial N_i}{\partial z}\left(\frac{\partial u}{\partial z}+\frac{\partial w}{\partial x}\right)\right\}}_{\text{diff } u}\mathrm{d}x\ \mathrm{d}y\ \mathrm{d}z$$

$$+\iint_{s}N_i\frac{(1+v_{\text{t,n}})}{Re}\left(\frac{\partial u}{\partial x}n_x+\frac{\partial v}{\partial x}n_y+\frac{\partial w}{\partial x}n_z\right)\mathrm{d}s.$$

The surface integral terms will vanish as either u is specified or $\partial u/\partial n=0$ at the surface. Thus, the x-momentum equation can be represented in a much simplified manner by

$$\iiint_{\forall} N_i\dot{u}\ \mathrm{d}x\ \mathrm{d}y\ \mathrm{d}z=-\iiint_{\forall}(\text{conv } u+\text{pgrd}u+\text{diff } u)\ \mathrm{d}x\ \mathrm{d}y\ \mathrm{d}z \tag{8}$$

In a similar way, the Galerkin's weighted residual equations of y- and z-momentum equations, respectively, may be written as

$$\iiint_{\forall} N_i\dot{v}\ \mathrm{d}x\ \mathrm{d}y\ \mathrm{d}z=-\iiint_{\forall}(\text{conv } v+\text{pgrd}v+\text{diff } v)\ \mathrm{d}x\ \mathrm{d}y\ \mathrm{d}z, \tag{9}$$

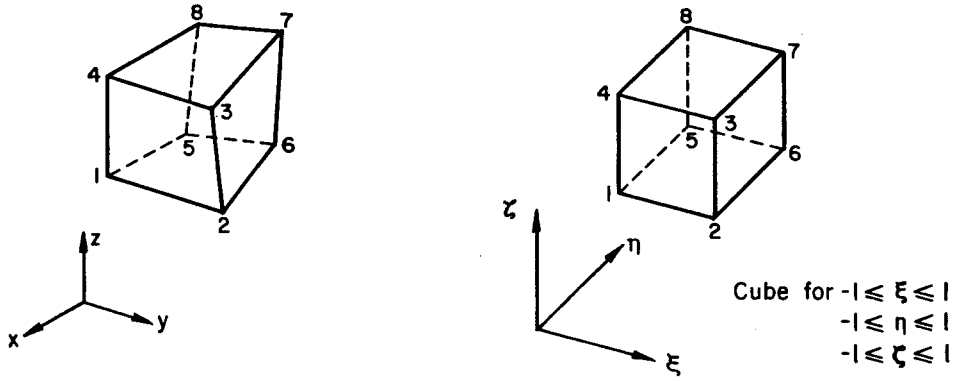

Figure 3. Transformation of a hexahedral element into a cube.

and

$$\iiint_{\forall} N_i \dot{w}\, \mathrm{d}x\, \mathrm{d}y\, \mathrm{d}z = -\iiint_{\forall} (\mathrm{conv}\, w + \mathrm{pgr}\mathrm{d}w + \mathrm{diff}\, w)\, \mathrm{d}x\, \mathrm{d}y\, \mathrm{d}z. \tag{10}$$

2.4. Shape functions

To interpolate the variable within an element (see Figure 3), isoparameteric formulation is used, i.e. the same shape functions are used for all variables

$$u = \sum_{j=1}^{8} N_j u_j, \qquad v = \sum_{j=1}^{8} N_j v_j, \qquad w = \sum_{j=1}^{8} N_j w_j, \qquad p = \sum_{j=1}^{8} N_j p_j,$$
$$x = \sum_{j=1}^{8} N_j x_j, \qquad y = \sum_{j=1}^{8} N_j y_j, \qquad z = \sum_{j=1}^{8} N_j z_j. \tag{11}$$

Usually the pressure variable is interpolated with polynomials that are one order less than those used for velocity field. This is done to avoid the ill conditioning of the coefficient matrix. However, this is necessary only for implicit schemes where matrix inversion is needed for evaluating the momentum equations. In the present study, however, the momentum equations are time stepped explicitly, and the velocity field is later adjusted for continuity by solving a Poisson equation for the pressure and velocity corrections. This approach may have a problem called a checkerboard pressure distribution, which slows down convergence considerably unless specific strategies are used to overcome it. In this algorithm even this problem is avoided due to reasons which will be explained subsequently. Even when this is not the case, equal order velocity–pressure formulation has been successfully used by some researchers [9,10].

To compute the elemental integrals the elements are mapped on a $2 \times 2 \times 2$ cube (Figure 3) in (ξ, η, ζ), and the shape functions are

$$N_1 = (1-\xi)(1-\eta)(1-\zeta)/8, \qquad N_2 = (1+\xi)(1-\eta)(1-\zeta)/8,$$
$$N_3 = (1+\xi)(1-\eta)(1+\zeta)/8, \qquad N_4 = (1-\xi)(1-\eta)(1+\zeta)/8,$$
$$N_5 = (1-\xi)(1+\eta)(1-\zeta)/8, \qquad N_6 = (1+\xi)(1+\eta)(1-\zeta)/8,$$
$$N_7 = (1+\xi)(1+\eta)(1+\zeta)/8, \qquad N_8 = (1-\xi)(1+\eta)(1+\zeta)/8,$$

where $-1 \le \xi \le 1,\ -1 \le \eta \le 1,\ -1 \le \zeta \le 1$.

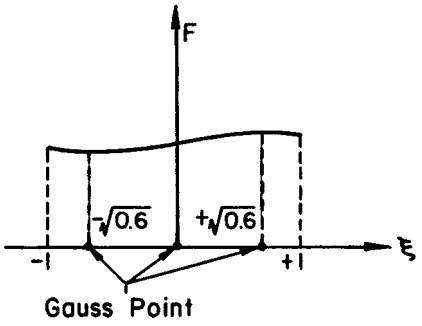

Figure 4. Location of Gauss points.

2.5. Numerical integration

In terms of normalized curvilinear co-ordinates, the elemental integrals take the form

$$\iiint_e (\ldots)\,\mathrm{d}x\,\mathrm{d}y\,\mathrm{d}z \equiv \int_{-1}^{1}\int_{-1}^{1}\int_{-1}^{1} (\ldots)|J|\,\mathrm{d}\xi\,\mathrm{d}\eta\,\mathrm{d}\zeta, \tag{12}$$

where the determinant of the Jacobian $|J|$ is the local volume scaling factor. The above integral can be integrated quite readily using simple integration techniques.

The Gauss–Legendre quadrature is used to numerically integrate Equation (12). Figure 4 illustrates discrete sampling points in each one of the three directions. The location of Gauss points and their weights are $(-\sqrt{0.6}, 0, \sqrt{0.6})$ and (5/9, 8/9, 5/9), respectively.

2.6. Evaluation of Cartesian derivatives

Global co-ordinates of a point are the functions of local co-ordinates ξ, η, ζ which can be represented as

$$x = x(\xi, \eta, \zeta), \qquad y = y(\xi, \eta, \zeta), \qquad z = z(\xi, \eta, \zeta). \tag{13}$$

The global co-ordinates of any point in an eight-noded cell can be represented in terms of the co-ordinates of the nodes by the expressions (Equation (11)) given before. These are used to evaluate the Jacobian matrix

$$\{J\} = \begin{bmatrix} x_\xi & y_\xi & z_\xi \\ x_\eta & y_\eta & z_\eta \\ x_\zeta & y_\zeta & z_\zeta \end{bmatrix} \tag{14}$$

where,

$$x_\xi = \frac{\partial x}{\partial \xi} = \sum_{i=1}^{8} \frac{\partial N_i}{\partial \xi} x_i, \qquad y_\xi = \sum_{i=1}^{8} \frac{\partial N_i}{\partial \xi} y_i \quad \text{and} \quad z_\xi = \sum_{i=1}^{8} \frac{\partial N_i}{\partial \xi} z_i, \tag{15}$$

and so on.

The Jacobian inverse can be written as follows

$$\{J\}^{-1} = \begin{bmatrix} \xi_x & \eta_x & \zeta_x \\ \xi_y & \eta_y & \zeta_y \\ \xi_z & \eta_z & \zeta_z \end{bmatrix}. \tag{16}$$

The Cartesian derivatives for any function ϕ can be written as

$$\begin{Bmatrix} \partial\phi/\partial x \\ \partial\phi/\partial y \\ \partial\phi/\partial z \end{Bmatrix} = \underbrace{\begin{bmatrix} \xi_x & \eta_x & \zeta_x \\ \xi_y & \eta_y & \zeta_y \\ \xi_z & \eta_z & \zeta_z \end{bmatrix}}_{\{J\}^{-1}} \begin{Bmatrix} \partial\phi/\partial\xi \\ \partial\phi/\partial\eta \\ \partial\phi/\partial\zeta \end{Bmatrix} \tag{17}$$

Finally the quantities such as $\partial u/\partial x$, $\partial v/\partial x$,..., $e$tc. are evaluated, by computing J^{-1} as described. Once these derivatives are computed at the Gauss points, the integrals in Equations (8)–(10) can be evaluated element by element.

2.7. Momentum equations assembly

Now solving Equation (8) implies

$$\sum_{e=1}^{n\,\mathrm{elem}} \iiint_{\forall} N_i \dot{u}\, \mathrm{d}x\, \mathrm{d}y\, \mathrm{d}z = -\sum_{e=1}^{n\,\mathrm{elem}} \underbrace{\left[\iiint_{\forall} (\mathrm{conv}\, u + \mathrm{pg}\, r\, \mathrm{d}u + \mathrm{diff}\, u)\, \mathrm{d}x\, \mathrm{d}y\, \mathrm{d}z \right]}_{t\mathrm{der}u},$$

where n elem is total number of elements in the domain, or

$$\dot{u}_i \sum_{n_i} \mathrm{coeff}_i = -\sum_{n_i} t\mathrm{der}u_i, \tag{18}$$

in which

$$\mathrm{coeff}_i = \iiint_{\forall} N_i\, \mathrm{d}x\, \mathrm{d}y\, \mathrm{d}z,$$

and n_i are the elements which have grid i as a node. Then, at each node i, the contribution from the neighboring elements will yield

$$g\ \mathrm{coeff}_i = \sum_{n_i} \mathrm{coeff}_i,$$

and

$$gt\mathrm{der}u_i = -\sum_{n_i} t\mathrm{der}u_i.$$

Similarly, solving Equations (9) and (10) at each node implies

$$gt\mathrm{der}v_i = \sum_{n_i} t\mathrm{der}v_i, \tag{19}$$

and

$$gt\mathrm{der}w_i = -\sum_{n_i} t\mathrm{der}w_i. \tag{20}$$

At each node i, we get

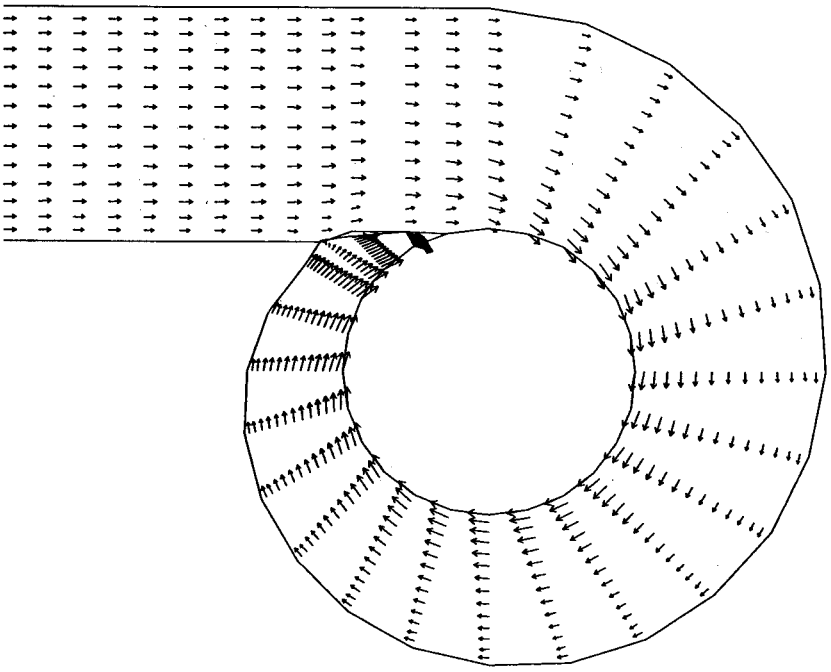

Figure 5. Velocity vectors on a horizontal midplane for $Re = 8 \times 10^5$.

$$\left.\begin{aligned} \dot{u}_i &= (gt\,\mathrm{der}u)_i/(g\ \mathrm{coeff})_i \\ \dot{v}_i &= (gt\,\mathrm{der}v)_i/(g\ \mathrm{coeff})_i \\ \dot{w}_i &= (gt\,\mathrm{der}w)_i/(g\ \mathrm{coeff})_i \end{aligned}\right\}. \tag{21}$$

Integrating in time leads to

$$\left.\begin{aligned} u_i^* &= u_i^n + (\dot{u}_i)\Delta\tau \\ v_i^* &= v_i^n + (\dot{v}_i)\Delta\tau \\ w_i^* &= w_i^n + (\dot{w}_i)\Delta\tau \end{aligned}\right\}, \tag{22}$$

where the superscript n denotes the nth time level and * denotes the provisional value at the $(n+1)$th time level. At the nth step, p^{n+1} is not known and hence Equation (22) predicts provisional velocities (instead of u_i^{n+1}, v_i^{n+1}, w_i^{n+1}) that satisfy the momentum balance using p^n as the first guess for p^*, the provisional value of p^{n+1}.

3. PRESSURE CORRECTION EQUATION

The pressure correction equation may be written as

$$\Delta\tau(\nabla^2 p') = \nabla \cdot \mathbf{v}^*, \tag{23}$$

where p' is $p^{n+1} - p^*$, and $\mathbf{v}^*$ is the provisional velocity vector. Equation (23) can now be further simplified using the weighted residual method

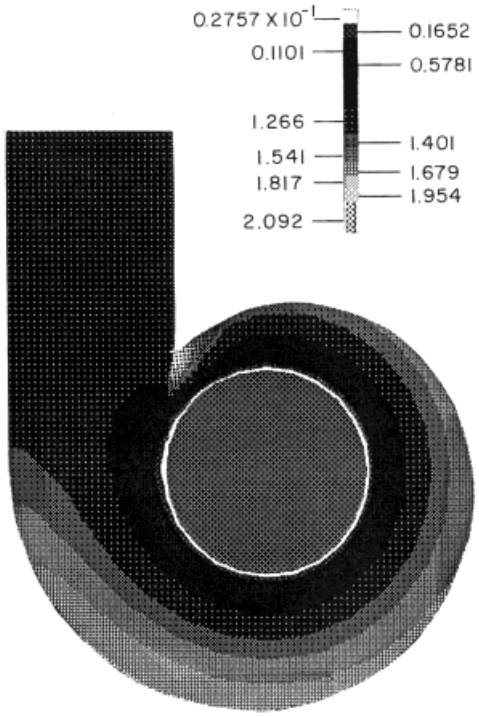

Figure 6. Pressure distribution at the midplane for $Re = 8 \times 10^5$.

$$\iiint_{\forall} N_i \Delta\tau(\nabla^2 p')\,\mathrm{d}x\,\mathrm{d}y\,\mathrm{d}z = \iiint_{\forall} N_i \nabla\cdot\mathbf{v}^*\,\mathrm{d}x\,\mathrm{d}y\,\mathrm{d}z.$$

The following is obtained using Green's theorem and integration by parts

$$\left[\iiint_{\forall}\left(\frac{\partial N_i}{\partial x}\frac{\partial N_j}{\partial x}+\frac{\partial N_i}{\partial y}\frac{\partial N_j}{\partial y}+\frac{\partial N_i}{\partial z}\frac{\partial N_j}{\partial z}\right)\mathrm{d}x\,\mathrm{d}y\,\mathrm{d}z\right]\{p'_j\} = \underbrace{-\frac{1}{\Delta\tau}\iiint_{\forall} N_i(\nabla\cdot\mathbf{v}^*)\,\mathrm{d}x\,\mathrm{d}y\,\mathrm{d}z}_{\text{res}}. \tag{24}$$

Equation (24) can again be decomposed into elemental equations (with 8×8 matrices) which are assembled in order to solve the global set of equations to get the pressure corrections p'. Note that the volume integral on the right side of Equation (24) is not converted to a surface integral (by using; Green's Theorem) as is often done in finite difference methods. Thus, the pressure–velocity decoupling in the element is avoided. This prevents a checkerboard pressure distribution from developing.

Once p' is calculated, the velocity corrections can be evaluated as

$$\mathbf{v}' = -\Delta\tau\nabla p'. \tag{25}$$

Finally, the updated values of u, v, w and p are obtained iteratively in the following way

$$\left.\begin{aligned} p^{n+1} &= p^* + p' \\ u^{n+1} &= u^* + u' \\ v^{n+1} &= v^* + v' \\ w^{n+1} &= w^* + w' \end{aligned}\right\}. \tag{26}$$

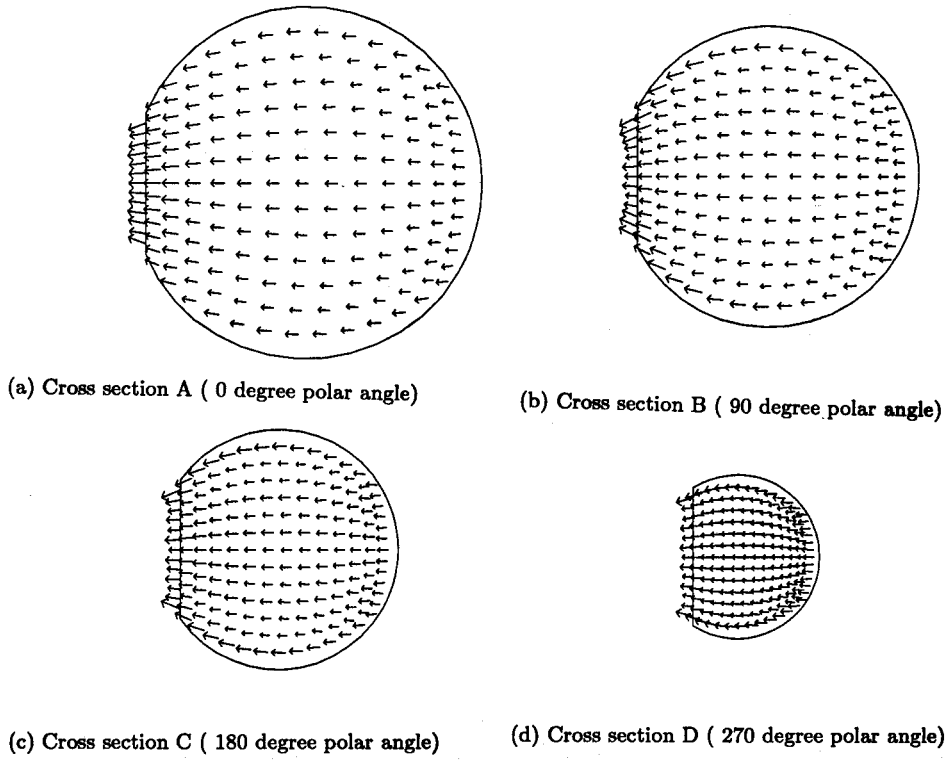

Figure 7. Secondary flow at the different cross sections for $Re = 8 \times 10^5$.

Computations progress in a time direction until a steady state situation is reached. The typical CPU time required for a $38 \times 15 \times 15$ grids is ≈ 22 h on a DEC-3000/400 S machine for a Reynolds number of 8×10^5. For the same Reynolds number and for a mesh size of $76 \times 21 \times 21$, the CPU time on a DEC-3000/400 S machine was 64 h. The circumferential distribution of static pressure for the above two cases were compared and the maximum difference was found to be $< 4\%$. Since the computational time with $76 \times 21 \times 21$ grids is nearly three times that with $38 \times 15 \times 15$ grids, computation with $76 \times 21 \times 21$ grids is abandoned in favour of $38 \times 15 \times 15$ grids.

4. RESULTS AND DISCUSSIONS

Figure 5 shows the velocity vectors at the horizontal midsection of the casing in the main stream direction for a Reynolds number of 8×10^5. It is evident from the velocity vectors that a uniform velocity profile at the entry finally culminates as a free vortex profile within the casing. The midplane velocity vectors are in good agreement with the results of Shyy and Vu [4]. The static pressure distribution for the Reynolds number of 8×10^5 is shown in Figure 6, which shows that the static pressure decreases towards the inner radius. This is in agreement with the free vortex motion at this plane. The pressure distribution is reasonably even. In this context, the work of Vu and Shyy [2] can be referred to, i.e. the use of a finite volume algorithm with $95 \times 21 \times 13$ grids for the configuration of interest. A pressure distribution plot presented by Vu and Shyy [2] shows a wavy pattern near the outside wall. It may be mentioned

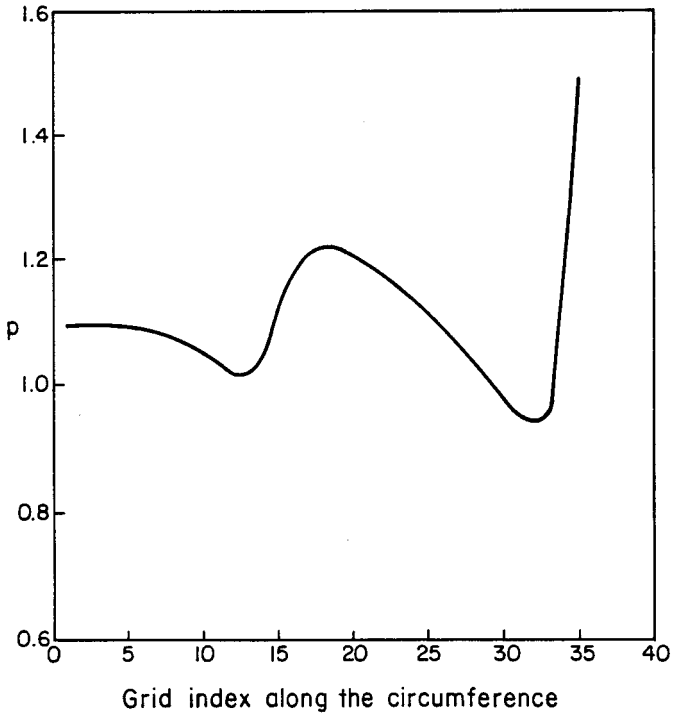

Figure 8. Static pressure distribution along the circumferential direction for $Re = 8 \times 10^5$.

that no such waviness in the pressure distribution is seen in Figure 6. In the present mathematical formulation, the pressure variable is interpolated in such a way that it becomes continuous across elements. The velocity vectors corresponding to secondary flow for the same Reynolds number at different cross-stream planes are shown in Figure 7. At the beginning of the turn, the flow over the cross-section plane A (Figure 7(a)) is evenly distributed and it is accelerated from the rear-end side to the exit. After a first 90° turn at the cross-stream plane B (Figure 7(b)), it is observed that the radial component is reasonably strong near the top and bottom of the casing and very weak near the centre of the casing. After a 180° turn at the cross-section C (Figure 7(c)), a similar structure of secondary flow is discerned. After a 270° turn (Figure 7(d)), the secondary flow is accelerated even more, which is revealed by the flow structure at the cross-section D. The development of the secondary flow observed in this investigation qualitatively reveals the results of Kurokawa and Nagahara [11]. Figure 8 shows the circumferential distribution of static pressure for the Reynolds number of 8×10^5 at the middle of the cross section. The first part of the casing is basically a circular duct, which entails very little decrease in pressure in the streamwise direction. As the spiral starts to bend, the wall curvature sets a pressure gradient in each section. This results in an increasing pressure along the circumferential direction. However, in the sections following the 20th section of the spiral casing, the pressure decreases rather sharply due to the accelerating flow out of the casing. The trend continues till 32nd section. The flow is blocked abruptly at the last section, which converts the kinetic energy into pressure, so there is a steep rise in pressure which starts increasing from 33rd section and attains maximum value at the end section.

5. CONCLUSIONS

The design of the optimum configuration of a spiral casing is an increasingly important concern of turbine manufacturers. The use of a CFD tool has been felt over the past decade. The present investigation forms a building block towards the development of such a computer code. Three-dimensional flow and pressure distribution in the casing have been obtained and results show a good quantitative agreement with experimental results. The development of a model for such a complex geometry establishes the capacity of the numerical method. The contribution of this investigation is in the successful application of a numerical method to an otherwise difficult engineering problem. Rigorous code validation with quantitative experimental results may be studied in the future.

APPENDIX A. NOMENCLATURE

D	diameter of the inlet section
e	elements
J	Jacobian
m	number of nodal points for each element
N_i	weighting function and shape function
P	static pressure
p	non-dimensional static pressure
Re	Reynolds number, $\rho W_0 D/\mu$
t	time
W_0	inlet velocity
U, V, W	velocities in the X-, Y- and Z-direction
u, v, w	non-dimensional velocities in the x-, y- and z-direction
X, Y, Z	dimensions in three directions
x, y, z	co-ordinates in three directions (normalized by characteristic length)

Greek symbols

v	kinematic viscosity of the fluid
$v_{t,n}$	non-dimensional turbulent kinematic viscosity
ρ	density of the fluid
τ	non-dimensional time
ξ, η, ζ	normalized local co-ordinates

Subscripts

$\forall$	volume of the computational domain
s	surface area of the computational domain
n	surface normal
w	wall
x, y, z	partial derivatives with respect to x, y, z
ξ, η, ζ	partial derivatives with respect to ξ, η, ζ

Superscripts

$\cdot$	partial derivative with respect to time
n	nth level time step
*	values obtained from momentum equation (provisional values)
$'$	corrections

REFERENCES

1. D. Ulrich, 'Berechnung der laminaren Stromung in einem Turbinenspiralgehause miltels einer Finite Element Formulierung der Navier–Stokes Gleichungen in nicht druckintergrierter Form', *Archive App. Mech.*, **56**, 192–200 (1986).
2. T.C. Vu and W. Shyy, 'Viscous flow analysis as design tool for hydraulic turbine components', *J. Fluids Eng. ASME*, **112**, 5–11 (1990).
3. T.C. Vu and W. Shyy, 'Navier–Stokes flow analysis for hydraulic turbine draft tubes', *J. Fluids Eng. ASME*, **112**, 199–204 (1990).
4. W. Shyy and T.C. Vu, 'Modeling and computation of flow in a passage with 360-degree turning and multiple airfoils', *J. Fluids Eng. ASME*, **115**, 103–108 (1993).
5. Z. Mrsa, 'Optimal design of spiral casing tongue and wicket gate angle by decomposition method', *Int. j. numer. methods fluids*, **17**, 995–1002 (1993).
6. F. Gomes Soares, A. Mesquita, G. Ciocan and J.L. Kueny, 'Numerical and experimental analysis of the flow in a pump-turbine spiral casing in pump operation', *XVII IAHR symposium*, Beging, China, 1994, pp. 249–258.
7. C. Taylor and T.G. Hughes, *Finite Element Programming of the Navier Stokes Equations*, Pineridge Press, UK, 1981.
8. T. Sundararajan, 'Automatic grid generation for complex geometry problems', in K. Muralidhar and T. Sundararajan (eds.), *Computational Fluid Flow and Heat Transfer*, Narosa Publishing House, New Delhi, 1995, pp.459–510.
9. J.G. Rice and R.J. Schinpke, 'An equal-order velocity–pressure formulation that does not exhibit spurious pressure models', *Comp. Meth. Appl Mech Eng*, **58**, 135–149 (1986).
10. D.L. Hill and E.A. Baskharone, 'A multiblock Navier–Stokes algorithm using equal-order quadratic finite elements', *Int. j. numer. methods fluids*, **20**, 169–185 (1995).
11. J. Kurokawa and H. Nagahara, 'Flow characteristics in spiral casing of water turbine', IAHR Symposium, vol. 2, *Paper no. 62*, Montreal, Canada, 1986.

